Coexistence of Gaussian and non-Gaussian statistics in vector integrable turbulence

Zhi-Yuan Sun,[1,3] Xin Yu,[1,*] and Yu-Jie Feng[2]

[1]*Institute of Fluid Mechanics, Beihang University, Beijing 100191, China*
[2]*Institute of Fundamental and Interdisciplinary Sciences, Beijing Union University, Beijing 100101, China*
[3]*International Research Institute for Multidisciplinary Science, Beihang University, Beijing 100191, China*

Integrable turbulence studies the complex dynamics of random waves for the nonlinear integrable systems, and it has become an important element in exploring the sophisticated turbulent phenomena. In the present work, based on the coupled nonlinear Schrödinger models, we have shown the coexistence of Gaussian and non-Gaussian single-point statistics in multiple wave components, which might be viewed as an exclusive feature for the vector integrable turbulence. This coexistent statistic can relate to different distributions of the vector solitonic excitations depending on the time-invariant nonlinear spectra. Our results are expected to shed light on a deeper understanding of the turbulent behaviors of vector waves and may motivate relevant experiments in the coupled optical or atomic systems.

I. INTRODUCTION

Integrable nonlinear partial differential equations, such as the celebrated Korteweg-de Vries and nonlinear Schrödinger equations, appear as a type of unique systems that are characterized by an infinite number of conserved quantities, with the dynamical behaviors confined on some particular surfaces in the phase space [1–4]. These equations, at the leading order, describe the nonlinear wave phenomena in many branches of physics including hydrodynamics, nonlinear optics, condensed matters and so on. In principle, integrable equations can be solved by using the inverse scattering transform (IST) [1], also known as the nonlinear Fourier transform, and a fascinating solution coined the name *soliton* has attracted extensive interest. This wave-natured entity transports and interacts with its profile unchanged, presenting the particlelike property.

When a random wave field contains a large ensemble of interacting solitons with certain parameter distribution, it can be linked to the concept *soliton gas*, first introduced by Zakharov [5,6]. It was an analog to the gas of interacting particles in the statistical mechanics. This concept is usually dedicated to the statistical understanding of a collection of solitons in integrable systems, on the contrary, for nonintegrable systems the term *soliton turbulence* [7] was suggested to reveal some different behaviors such as the incoherent soliton turbulence [8].

More recently, the terminology *integrable turbulence* (IT) was introduced for studying the complex dynamics of random waves in nonlinear integrable systems [9], and it has attracted much attention from the theoretical and experimental communities [10–15]. Roughly speaking, IT includes two aspects: One is the weakly interacting wave turbulence [16], and the

other one is for the strong turbulence where nonlinear localized modes such as solitons or breathers dominate [11–13]. The latter may further relate to the theory of soliton gas. Although specific, IT may serve as a valuable direction for better understanding the sophisticated turbulent phenomena to some extent.

A ubiquitous integrable model as the paradigm of studying IT is the scalar one-dimensional nonlinear Schrödinger equation (NLSE) with focusing nonlinearity. The turbulent dynamics of this equation is determined by the initial condition, and its IST spectrum is invariant as the time evolves. Here we shall mention two typical random initial conditions [17]: (i) the noisy perturbation of a plane wave that triggers the modulation instability (MI) process [18]; (ii) the partially coherent waves with a narrow Fourier spectrum that experience self-focusing interaction [15,19]. Both conditions result in a random wave field characterized by a stationary single-point statistics for the long-time evolution. This stationary state contains numbers of highly nonlinear localized excitations, such as solitons and breathers, which move and interact on a background of small-amplitude radiation waves.

Surprisingly, the noise-driven MI leads to the Gaussian single-point statistics of the wave field at long times, with an exponential distribution of the wave intensities. This phenomenon has been observed in numerical simulations and optical experiments, but its rigorous proof is still open [11,12,17,18,20]. Alternatively, the Gaussian-distributed partially coherent waves can induce a non-Gaussian statistics of the long-time wave field with the heavy-tailed intensity distribution [14,15,21,22]. Such a distribution is the sign of probabilistic increase of the so-called rogue waves (RWs), some high-amplitude wave structures that emerge with low probability. This term was initially employed to label unexpected and destructive giant oceanic waves, but has now been generalized to represent large-amplitude waves in many physical systems [23–27].

*yuxin@buaa.edu.cn

Although there exist fruitful results on the scalar IT, especially within the framework of 1D NLSE, the study of the turbulent dynamics for the vector integrable systems is rather limited. On the one hand, those systems of coupled waves have their importance in describing the physical phenomena with two or more different components, with the applications in fluid dynamics, nonlinear optics, and Bose-Einstein condensates (BECs) [28–31]. On the other hand, the vector integrable systems, e.g., the vector NLSEs, present some unique features such as the energy transfer and redistribution between the coupled modes that may lead to various new types of vector solitonic solutions [32–37], as well as deterministic RW solutions [28,31,38]. These solutions have also been constructed for other vector systems including the three-wave resonant interaction equations [39] and the long-wave-short-wave resonance [40]. Hence, we have reasons to expect some exclusive statistical manifestation of the turbulent wave fields for the vector integrable systems. In the present work, a typical paradigm is provided for this purpose.

II. MODEL AND METHODS

We consider a dimensionless vector NLSE with two components, i.e., the well-known focusing Manakov equation [41],

$$i\frac{\partial \psi_1}{\partial t} + \frac{\partial^2 \psi_1}{\partial x^2} + 2(|\psi_1|^2 + |\psi_2|^2)\psi_1 = 0, \quad (1a)$$

$$i\frac{\partial \psi_2}{\partial t} + \frac{\partial^2 \psi_2}{\partial x^2} + 2(|\psi_1|^2 + |\psi_2|^2)\psi_2 = 0, \quad (1b)$$

where t is the evolution variable that plays the role of time, x is the transverse variable, and the complex wave functions $\psi_1(x, t)$ and $\psi_2(x, t)$ describe the physical fields of interest (e.g., those in water waves, nonlinear optics, BECs, etc. [28–31]). The initial value problem of this integrable model can be solved by using the IST method for appropriate boundary conditions [3], and various solitonic solutions can be constructed by means of the Hirota method and Darboux transformation [28,31,32,34].

To our knowledge, there are few statistical results on the relatively strong turbulence of Eq. (1), where the nonlinear coherent excitations such as solitons and breathers widely appear in the wave fields. References [42,43] considered the initial conditions as the weak-noise-perturbed plane waves in both modes, and found the long-time wave amplitudes to obey Gaussian distribution for both components; when the noisy perturbations become strong, both modes may display non-Gaussian distribution. This property in fact represents no essential difference from that of the scalar IT based on the single NLSE [12,13]. Here, for the Manakov model, we show a coexistence of Gaussian and non-Gaussian single-point statistics in the different components, which may be viewed as a unique feature for the vector IT.

For the above purpose, we employ the initial condition as a constant background of unit amplitude in one component and a partially coherent wave field for another component, namely,

$$\psi_1(x, 0) = 1, \quad \psi_2(x, 0) = f(x), \quad (2)$$

where $f(x)$ is a complex random function with its real and imaginary parts taking two independent Gaussian distributed
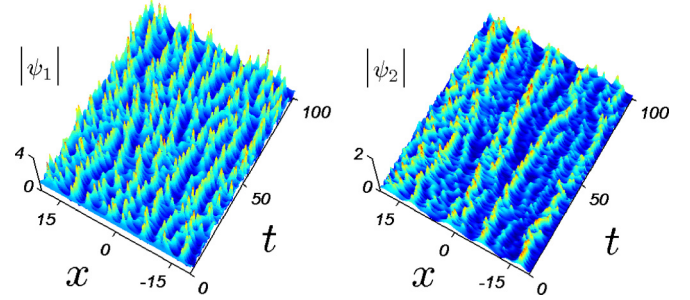

FIG. 1. Three-dimensional plots of parts of the turbulent wave fields $|\psi_1(x, t)|$ and $|\psi_2(x, t)|$ for a specific realization of $f(x)$, with $\sigma = 0.2$ and $l_c = 3$.

and Gaussian correlated random functions. They have zero mean and the same variance σ^2 and the same correlation length l_c. Thus, the intensity $|f(x)|^2$ follows an exponential distribution with $\langle |f(x)|^2 \rangle = 2\sigma^2$.

We performed extensive numerical simulations on Eq. (1) by using the fourth-order split-step method [3] in a periodic box of the size $L = 512\pi$, with a uniform grid of $N = 2^{15}$ nodes. The simulation was implemented up to $t_f = 400$ where the IT has developed to its stationary state in both components, and a tendency toward the Fermi-Pasta-Ulam-Tsingou recurrence [44] was not observed. We have checked our results by using different integration schemes and found no changes (a brief discussion on the numerical errors can be seen in Appendix A).

III. RESULTS AND DISCUSSIONS

A. Scintillation index

As a typical example, Fig. 1 presents part of the wave fields for a specific realization of $f(x)$. We see that both fields contain large numbers of nonlinear localized excitations (which will be classified as solitons and breathers). They move and interact on the background of small radiation waves. However, there appears obvious difference between the random patterns of the two components, which is a basic but universal character for the hundreds of realizations of simulation results that may result in different distributions of the wave amplitudes between components.

We introduce a single statistical quantity to describe the intensity fluctuations of the wave fields, the so-called scintillation index (SI) [45], defined as

$$\kappa_j(t) = \frac{\langle |\psi_j|^4 \rangle}{\langle |\psi_j|^2 \rangle^2} - 1, \quad j = 1, 2, \quad (3)$$

where the averages are taken over x direction as well as the different realizations of $f(x)$. This index is also named as the kurtosis [10], the normalized fourth-order moment of the wave amplitude $|\psi_j|$, which is efficient in characterizing RWs in turbulent wave fields [45–47]. Generally speaking, Gaussian statistics has a SI of unity, while $\kappa > 1$ implies a heavy-tailed distribution of the intensities where the waves are concentrated that may lead to a higher probability of RW formation.
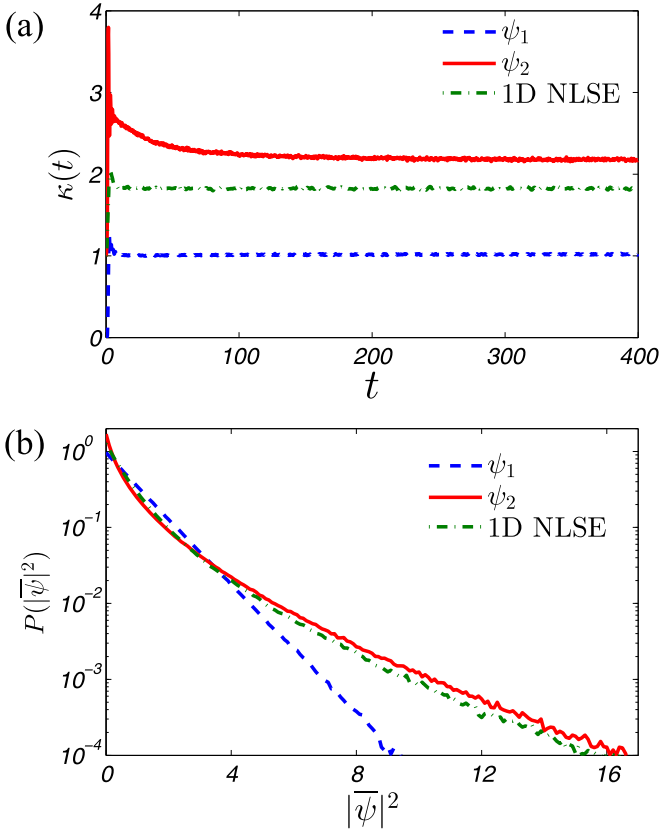
FIG. 2. (a) Scintillation indices κ, each averaged over 200 realizations of $f(x)$, as functions of t. (b) Probability density functions $P(|\overline{\psi}|^2)$ of the normalized wave intensities $|\overline{\psi}|^2$ at $t = 400$. The blue dashed line is for the mode ψ_1 and the red solid line is for the mode ψ_2. Accordingly, the results for the 1D scalar NLSE (the green dot-dashed lines) are given with $\psi_2(x, 0)$ as the initial conditions. The parameters include $\sigma = 0.2$ and $l_c = 3$.

Figure 2 presents the main statistical findings for hundreds of simulations. Figure 2(a) shows the evolution of the SI with the time for both components. After a transient regime from the initial stage, $\kappa_{1,2}$ converges to a stationary regime and nearly does not change for $t > 200$ (more numerical evidences supporting the stationary regime can be found in Appendix B). Here the most interesting result is that κ_1 approaches to unity while κ_2 tends to a value larger than two, which explicitly reveals a coexistence of the Gaussian and non-Gaussian single-point statistics of wave amplitudes for the long-time propagation. More clearly, in Fig. 2(b) we display the probability density function of the normalized wave intensity $|\overline{\psi}_j|^2$ measured at $t_f = 400$ [the wave functions are normalized as $\psi_1 \rightarrow \overline{\psi}_1$ and $\psi_2/(\sqrt{2}\sigma) \rightarrow \overline{\psi}_2$]. Apparently, the component ψ_1 shows an exponential distribution and the component ψ_2 gives a heavy-tailed distribution with its tail more elevated. This implies that the probability of the occurrence of RWs is more increased for the second mode.

In addition, in this figure we also provide the results for the 1D scalar NLSE, i.e., Eq. (1) with the component ψ_1 vanished. Apparently the time evolution of κ_2 changes when the initial plane wave in ψ_1 is considered. For the short timescale, κ_2 of the scalar case has one maximum hump before tending

to the stationary regime [also see Fig. 3(c)], while for the vector case it contains several fast oscillations and a relatively slow decaying. For the long timescale, κ_2 of the vector case approaches a value larger than that of the scalar case, which means a higher probability of RW occurrence. This point can also be reflected from Fig. 2(b), where the PDF curve of ψ_2 is more elevated for the vector wave fields.

The transient regime of $\kappa(t)$ is further described in Fig. 3 representing the early stage of vector integrable turbulence. We display typical examples with increasing strength of the disorder. For enough small σ [see Fig. 3(a)], the vector system is decoupled (also explained in the following section), and ψ_1 behaves like the noise-induced MI of scalar NLSE [11,20], with κ_1 showing a decaying oscillations due to the phenomenon of recurrence. The component ψ_2 is nearly a linear field synchronized by the potential term $|\psi_1|^2\psi_2$. As σ increases, the oscillations are decreasing and not well synchronized [see Figs. 3(b) and 3(c)] since the coupling of the vector fields takes effect. However, κ_2 is very unlike the scalar case with only one maximum hump [48], instead it results from the mutual interaction between the recurrence-like behavior in ψ_1 and focusing effect in ψ_2. When σ is large enough, the oscillations of $\kappa(t)$ almost disappear and there presents a single hump [see Fig. 3(d)], where the focusing effect seems to dominate. After these fast oscillations (or one hump), the slow decaying of $\kappa_2(t)$ is a remarkable effect when $|\psi_2|$ is large enough to compete with $|\psi_1|$ [see Figs. 3(c) and 3(d)]. The decaying might be a result of this competition that can reduce the gap between κ_1 and κ_2. This argument is better verified in Fig. 3(d), where κ_1 shows a slow growth at the same time as κ_2 decays.

B. Parametric dependence

To see the dependence of the long-time wave statistics on the initial parameters (σ, l_c), we define the following time-averaged SI,

$$\overline{\kappa_j} = \frac{1}{t_f - t_0} \int_{t_0}^{t_f} \kappa_j dt \quad j = 1, 2, \qquad (4)$$

where $t_0 = 200$ is used, after which both components tend to the stationary states with nearly invariant values of SI (see the examples in Appendix B). For practical use, $|\overline{\kappa} - 1| < \varepsilon$ ($\varepsilon = 0.05$) was set as the criterion for the Gaussian single-point wave field; otherwise, the wave statistics was seen to obey the non-Gaussian distribution (in this work, we mainly dealt with the heavy-tailed distribution with $\overline{\kappa} > 1 + \varepsilon$). Figure 4(a) presents a diagram based on our extensive simulations. We found that, with σ increasing, the vector wave field transits from a coexistence of the Gaussian and non-Gaussian statistics to both non-Gaussian statistics. For the smaller correlation length $l_c < 2$, this transition appears to happen at the point with a bit larger σ. As a result we have confirmed a parameter regime where the Gaussian and non-Gaussian distributions of the wave fields can exist at the same time.

Here we emphasize that this regime still corresponds to the nonlinear coupling of the two components in Eq. (1). As a comparison, considering the enough small σ, we may have $|\psi_1(x)| \gg |\psi_2(x)|$ for $\forall x$ at any time such that the Manakov model is decoupled. The component ψ_1 has the similar
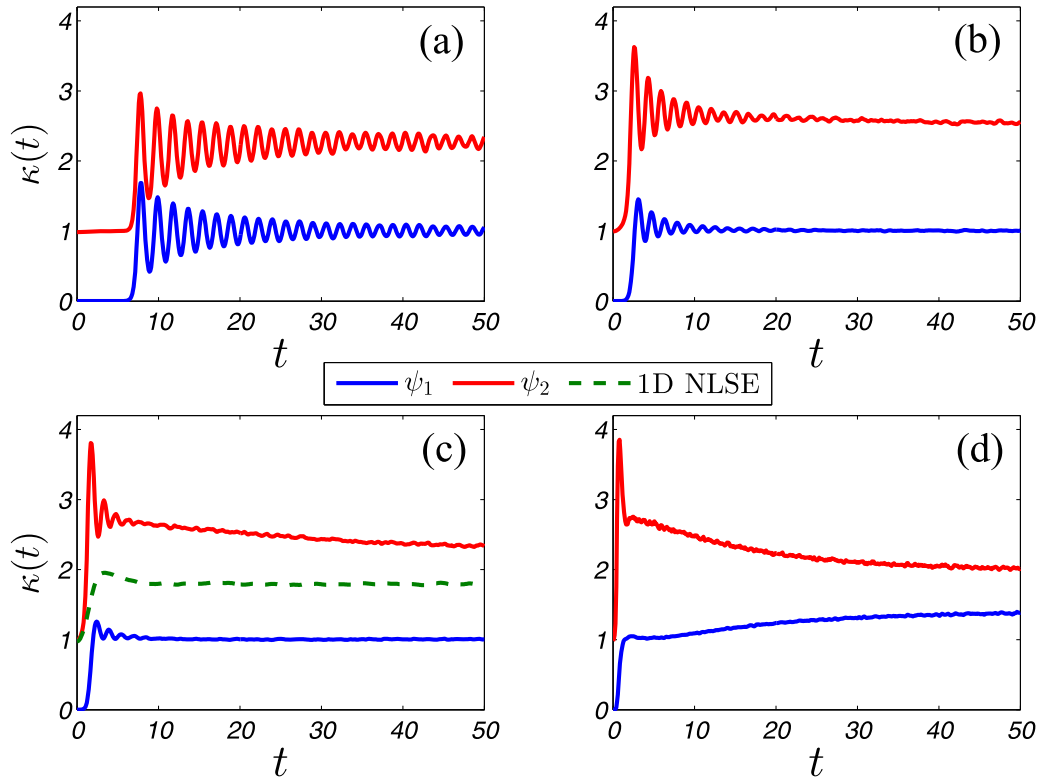
FIG. 3. Ensemble-averaged scintillation indices κ as functions of t for $l_c = 3$. (a) $\sigma = 0.001$; (b) $\sigma = 0.1$; (c) $\sigma = 0.2$; (d) $\sigma = 0.5$. The blue solid line is for the mode ψ_1 and the red solid line is for the mode ψ_2. In panel (c), $\kappa(t)$ for the scalar NLSE is given with the initial conditions chosen the same as $\psi_2(x, 0)$ of the vector case.

behavior as the weak-noise-driven MI for the scalar NLSE which shows the Gaussian statistics for the long-time propagation. The component ψ_2 becomes a linear system with the intensity $|\psi_1|^2$ as an external potential. The linear waves may also present the non-Gaussian distribution due to the concentration effect of this potential. However, this distribution of the normalized waves for the component ψ_2 does not change with σ because of its linear property.

Figure 4(b) gives an example showing the transition from the decoupled to the coupled regimes (Other cases have the

similar transient variations). Also in this figure we provide the time-averaged SI for the scalar NLSE as comparison [equivalent to the cases with $\psi_1(x, 0) = 0$ and $\psi_2(x, 0) = f(x)$]. When $\sigma \lesssim 10^{-3}$, the time-averaged SI is invariant in both components, corresponding to the regime of decoupled waves, as analyzed above. As $\sigma \gtrsim 10^{-3}$, $\overline{\kappa_2}$ begins to vary with σ, so the nonlinear coupling has taken effect. A regime $10^{-3} \lesssim \sigma \leqslant 0.26$ exists where $\overline{\kappa_1}$ nearly equals to unity while $\overline{\kappa_2}$ is obviously larger than one. This is the regime we say the coexistence of Gaussian and non-Gaussian distributions
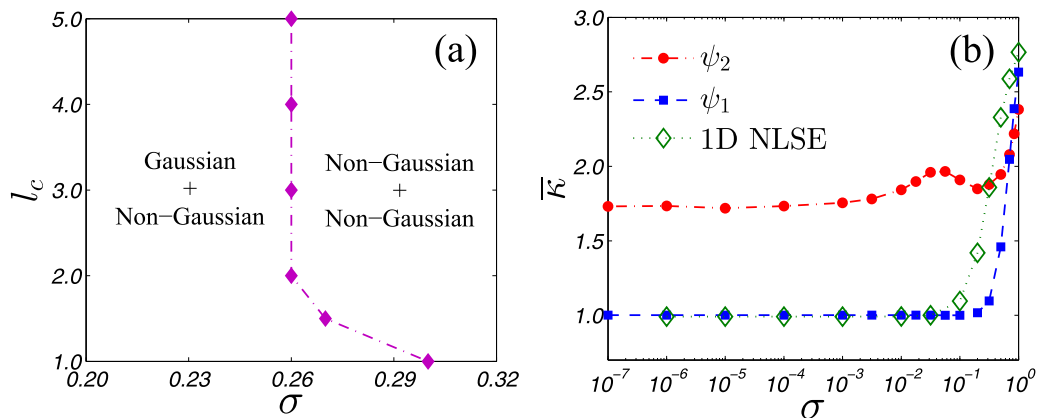

FIG. 4. (a) The diagram showing two different regimes, where the left regime is for the Gaussian statistics in the component ψ_1 and non-Gaussian statistics in the component ψ_2, while the right regime has the non-Gaussian statistics in both components. (b) Plots of $\overline{\kappa}$ with σ varying in several orders of magnitude ($l_c = 2.0$). The blue squares and red circles correspond to the components ψ_1 and ψ_2, respectively, while the green diamonds are for the scalar NLSE results.
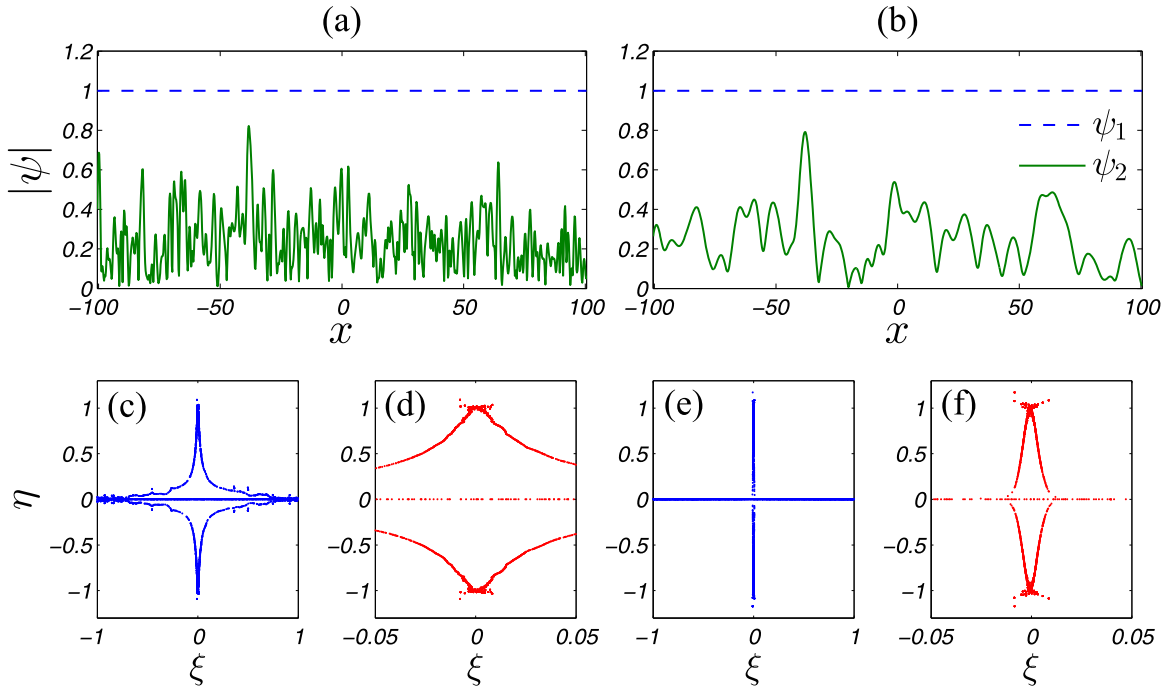
FIG. 5. Typical vector wave fields generated from the initial conditions (2) with $\sigma = 0.2$ and (a) $l_c = 1$; (b) $l_c = 5$. The corresponding global spectra calculated by the DK scheme are portrayed in panels (c) and (e), with the portions near the imagine axis zoomed in panels (d) and (f).

under the influence of nonlinear coupling. The varying trend of $\overline{\kappa_2}$ with σ in this regime is apparently different from that for the 1D scalar NLSE. It composes of an increasing and a decreasing intervals, which may be respectively due to the nonlinear focusing and the decaying effect as explained in Fig. 3. When $\sigma \gtrsim 0.26$, both components present non-Gaussian (heavy-tailed) distributions with $\overline{\kappa_{1,2}}$ monotonically increasing with σ, indicating a stronger nonlinear coupling.

C. Nonlinear spectral analysis

Now we turn to a deeper understanding of the nonlinear wave fields with localized coherent excitations by using the tool of IST. This technique decomposes the nonlinear waves into localized solitary eigenmodes and dispersive radiation components, which can be employed to study from single soliton to soliton ensembles in integrable systems [12,18,49], and even be effective for analyzing some nearly integrable systems with small perturbations [46,50–52].

The basis of the IST is to solve the Zakharov-Shabat spectral problem for a given vector wave field $[\psi_1(x, t), \psi_2(x, t)]$,

$$\frac{d\mathbf{Y}}{dx} = \begin{pmatrix} -i\lambda & 0 & \psi_1 \\ 0 & -i\lambda & \psi_2 \\ -\psi_1^* & -\psi_2^* & i\lambda \end{pmatrix} \mathbf{Y}, \tag{5}$$

where $\mathbf{Y}(x, t; \lambda)$ is a vector and $\lambda = \xi + i\eta \in \mathbb{C}$ represents the spectral eigenvalues, ξ and η are, respectively, the real and imaginary parts. For the integrable Manakov system, the spectrum of eigenvalues is invariant as the t variable evolves. These eigenvalues are symmetrically distributed on the upper and lower complex planes.

Generally speaking, there are two cases of interest. One case is for the localized wave fields with the intensity van-

ishing at the boundaries. Such that a typical eigenvalue apparently away from the real and imaginary axes corresponds to the vector soliton, and its total intensity is four times $|\eta|$ while its velocity is associated with ξ. The eigenvalues that appear very near the real axis stand for linear radiation waves with small amplitudes.

Another case is for the periodic boundary conditions, which is used in our study. The spectral properties of this case can be analyzed by Floquet theory [4,53–56]. This theory tells that all bounded solutions of Eq. (5) can be written in the form

$$\mathbf{Y}(x) = e^{i\gamma x}\hat{\mathbf{Y}}(x), \tag{6}$$

where $\gamma \in \mathbb{R}$ is the Floquet exponent and $\hat{\mathbf{Y}}(x)$ has the basic period L along x coordinate, i.e., $\hat{\mathbf{Y}}(x + L) = \hat{\mathbf{Y}}(x)$. Equation (6) shows that

$$\mathbf{Y}(x + L) = e^{i\gamma L}\mathbf{Y}(x). \tag{7}$$

Therefore, the full spectrum is derived with the Floquet exponent as a parameter

$$\gamma \in \left[0, \frac{2\pi}{L}\right). \tag{8}$$

Similar to the scalar NLS case, the main spectrum corresponds to the special values $\gamma = 0$ and $\gamma = \frac{\pi}{L}$ that are for the periodic and antiperiodic eigenfunctions, respectively. Substituting the Floquet equation (6) into Eq. (5), we rewrite the eigenvalue problem as follows:

$$\begin{pmatrix} i\partial_x - \gamma & 0 & -i\psi_1 \\ 0 & i\partial_x - \gamma & -i\psi_2 \\ -i\psi_1^* & -i\psi_2^* & -i\partial_x + \gamma \end{pmatrix} \hat{\mathbf{Y}} = \lambda\hat{\mathbf{Y}}. \tag{9}$$

Since $\hat{\mathbf{Y}}$ is periodic, We can numerically solve the spectral problem (9) by using the Fourier collocation (FC) method [3,49] with periodic boundary conditions. Each choice of the Floquet exponent γ in Eq. (8) results in the eigenvalues constituting part of the spectrum. This type of algorithm, also known as Deconinck-Kutz (DK) scheme [57], is efficient for solving the nonlinear spectral problems with periodic potentials [58,59]. The spectrum can also be analyzed by employing a numerical IST procedure with a spatial periodization of the wave field under consideration [60]. An example is given in Appendix C to show that both methods can produce the spectral distribution effectively. Appendix D demonstrates that our methods work correctly on some known solitonic solutions of Eq. (1).

Figures 5(a) and 5(b) present two typical wave fields given by Eq. (2) with the same $\sigma = 0.2$ but different l_c (note that only the partial simulation domain was displayed for clarity). The corresponding global spectra for the periodic waveforms are given in Figs. 5(c)–5(f). For both wave fields, we see a large complex conjugate loop dominating the spectrum distribution, which is much wider for smaller l_c. There are many small-amplitude loops crossing the real axis that can be viewed as being perturbative for $l_c = 1$, but these structures are hardly seen for $l_c = 5$. Additionally, we found that lots of small-size loops (some of them are pointlike) concentrate near the point $(\xi, \eta) = (0, \pm1)$, and they may correspond to the solitonlike objects. In various realizations of randomness, the composition of the spectral portraits appear to be similar when σ and l_c are the same as in Fig. 5.

As to multiple realizations of the initial conditions, the statistical distribution of the main spectral eigenvalues on the complex plane was given in Fig. 6 for two typical cases with the same σ but different l_c. Here, the probability density function $p(\xi, \eta)$ represents the eigenvalue distribution of main spectra, and $p(\xi, \eta)d\xi d\eta$ is the probability of eigenvalues found in the spectral element $\lambda \in [\xi, \xi + d\xi] \times [\eta, \eta + d\eta]$. Note that we only recorded the eigenvalues with $|\eta| > \varepsilon$ ($\varepsilon = 0.05$) to avoid the linear radiation waves with very small amplitudes, and in this figure we plot $\log_{10}[p(\xi, \eta)]$ for a clearer view of the density functions with their values covering different orders of magnitudes. The function $p(\xi, \eta)$ was normalized as $\int_{-\infty}^{+\infty} d\xi \int_{\varepsilon}^{+\infty} d\eta \, p(\xi, \eta) = 1$.

Although both cases in Fig. 6 support the coexistence of Gaussian and non-Gaussian statistics [see in Fig. 4(a)], their eigenvalue distributions of main spectra form distinct global shapes that depend on the correlation length. For $l_c = 1$ [see Fig. 6(a)], many eigenvalues locating at the lower positions (with smaller $|\eta|$) have sufficiently large real parts which means that the corresponding nonlinear excitations have acquired significant velocities. The eigenvalues at the higher positions (with larger $|\eta|$) own neglectable (much smaller) real parts. In contrary, for $l_c = 5$ [see Fig. 6(b)], all the eigenvalues are almost distributed adjacent to the imaginary axis. Figures 6(c) and 6(d) portray the local vision of the main spectra very near the imaginary axis, which clearly show the spectral expansion along ξ depending on the correlation length l_c. To further compare the distribution of the imaginary parts of those eigenvalues, we individually look at in Fig. 6(e) the probability density function of η, defined as $p(\eta) = \int_{-\infty}^{+\infty} p(\xi, \eta)d\xi$. We found the distribution almost the
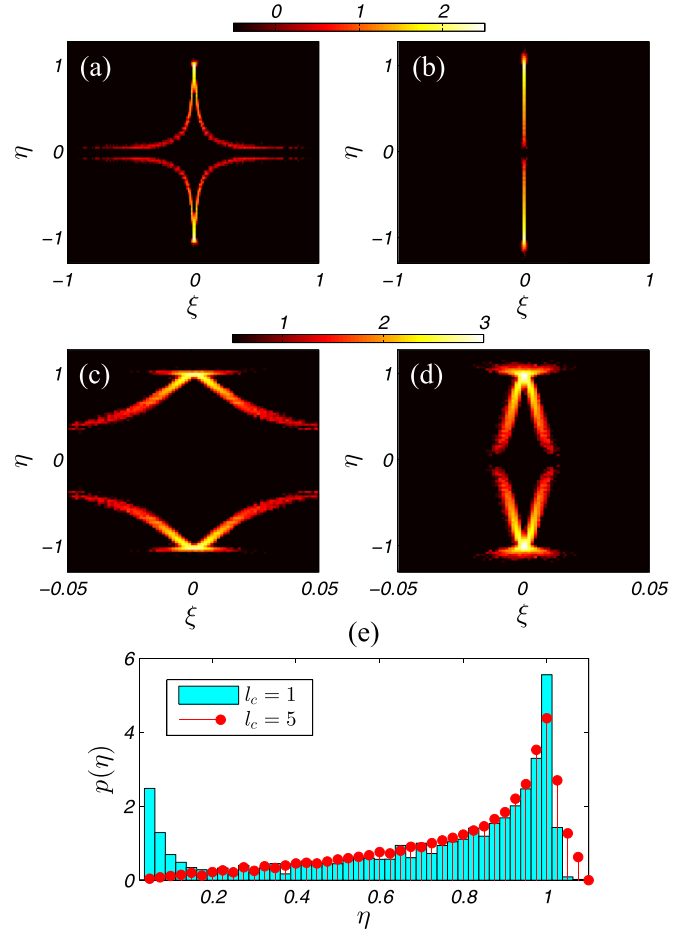

FIG. 6. Logarithm plots of the probability density functions $\log_{10}[p(\xi, \eta)]$ for the main spectral eigenvalues with $\sigma = 0.2$ and (a) $l_c = 1$; (b) $l_c = 5$. The statistics was taken from 100 realizations of the initial conditions. Corresponding to panels (a) and (b), panels (c) and (d) portray the zoomed areas adjacent to the imaginary axis with finer plot grids. (e) Probability density functions $p(\eta)$ showing the distribution of the imaginary parts of the eigenvalues for panels (a) and (b). Note that we only consider $\eta > 0$ due to the symmetric distribution of the eigenvalues.

same except for two regions $\eta \lesssim 0.2$ and $\eta \gtrsim 1.0$. In these regions, the smaller l_c increases the ratio of small nonlinear excitations and linear radiation waves with $\eta < 0.2$, while the larger l_c increases the percentage of large vector solitonlike entities with $\eta > 1.0$. Thus, we get the point that, for certain range of the parameters, variation of the correlation length can apparently change the wave contents (revealed from the distribution of the main spectra), but the coexistence of Gaussian and non-Gaussian distributions is preserved. We stress that the nonlinear spectra for the Manakov model are very different from those for the scalar NLS equation, as explained in Appendix E.

We notice that for the focusing Manakov equations with nonzero boundary conditions, Ref. [36] has found three different types of IST eigenvalues, where the first type corresponds to the trivial vectorization of the breather solutions of the scalar NLS equation, while the second and third types are the analog of the distinct dark-bright soliton
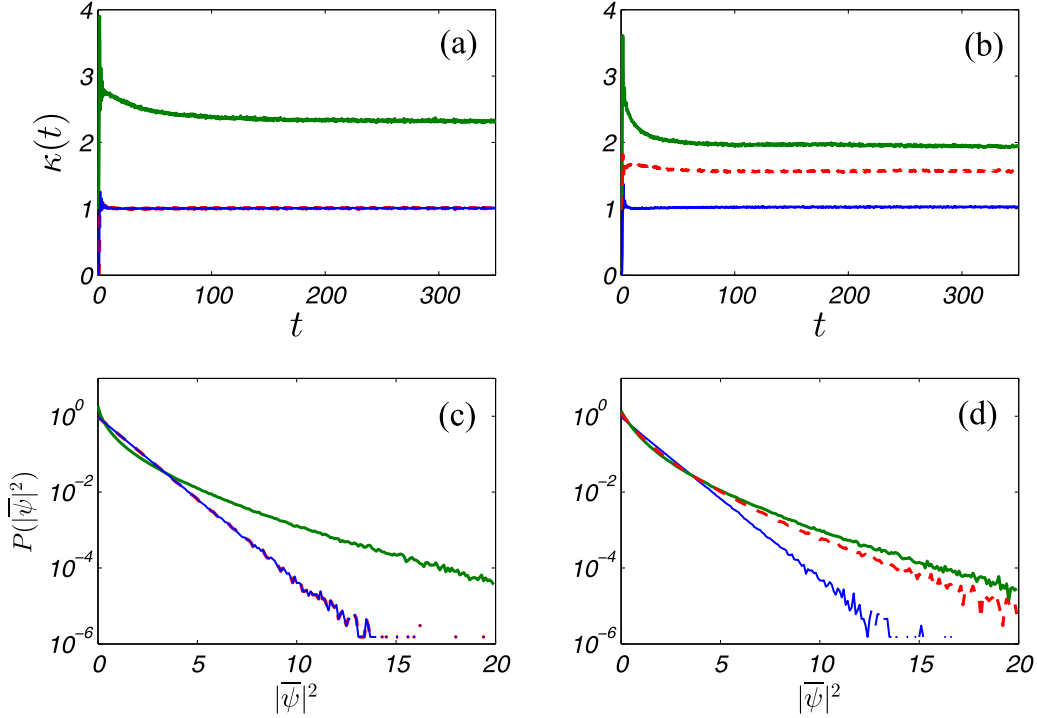
FIG. 7. Scintillation indices κ as functions of t: (a) $\psi_1(x,0) = 1$, $\psi_2(x,0) = 0.6$, and $\psi_3(x,0) = f(x)$ with $\sigma = 0.2$ and $l_c = 3$; (b) $\psi_1(x,0) = 1$, $\psi_2(x,0) = f_1(x)$ with $\sigma = 0.2$ and $l_c = 1$, and $\psi_3(x,0) = f_2(x)$ with $\sigma = 0.2$ and $l_c = 3$. Corresponding to panels (a) and (b), the probability density functions $P(|\overline{\psi}|^2)$ of the normalized wave intensities $|\overline{\psi}|^2$ at $t = 350$ are displayed in panels (c) and (d). For all panels, the blue solid line, red dashed line, and green solid line are for the components ψ_1, ψ_2, and ψ_3, respectively.

solutions. The multisoliton solutions containing a combination of the three types of eigenvalues may display resonant interactions among them [37]. Here our global distribution of eigenvalues is based on the periodic boundary conditions, and how their locations on the complex plane of the spectra relate to the three types of eigenvalues for the nonzero boundary conditions on the whole line should be an open question.

IV. GENERALIZATION AND SUMMARIES

Till now we have realized the Gaussian plus non-Gaussian statistics in a two-component IT that contains large numbers of nonlinear solitonic excitations. Naturally one may wonder whether the similar combined distributions exist in the N-component integrable system with $N > 2$. So we would consider a generalization of the Manakov model (1)

$$i\frac{\partial \Psi}{\partial t} + \frac{\partial^2 \Psi}{\partial x^2} + 2\|\Psi\|^2 \Psi = 0, \qquad (10)$$

where Ψ is a N-component vector $\Psi = (\psi_1, \psi_2, \cdots, \psi_N)$, and $\|\cdot\|$ is the Euclidean norm as $\|\Psi\|^2 = \sum_{j=1}^{N} |\psi_j|^2$. This model is integrable by the IST [61]. Here, we report a simulation example for $N = 3$, as shown in Fig. 7. Using the appropriate initial conditions of the similar types as Eq. (2), this instance realizes at the long times two different combinations of the single-point wave statistics: (i) the Gaussian distribution for two components and the non-Gaussian distribution for the third component [see Figs. 7(a) and 7(c)]; (ii) the non-Gaussian distribution for two components and the

Gaussian distribution for the third component [see Figs. 7(b) and 7(d)]. This realization indicates that the exponential and heavy-tailed wave intensity distributions can coexist at least in a three-component IT, with its combination presenting some diversity.

In summary, by studying the turbulent wave behaviors of the two-component Manakov model, we have revealed a unique feature for the vector integrable turbulence, namely, the coexistence of Gaussian and non-Gaussian single-point statistics for the long-time evolution. This nontrivial property can be observed for a range of initial parameters, which correspond to the effective coupling of the nonlinear wave fields. The nonlinear spectral analysis further shows that the distribution of the solitonic coherent excitations may be changed with the Gaussian plus non-Gaussian statistics preserved. We also provide the evidence that the similar combined distributions can be realized for the integrable three-component NLSEs. We hope to open up a new gate for the theoretical investigation on vector integrable turbulence, and also expect future realizations of our results in the relevant experiments such as those in multimode optical fibers and coupled BEC systems [29,30,62].
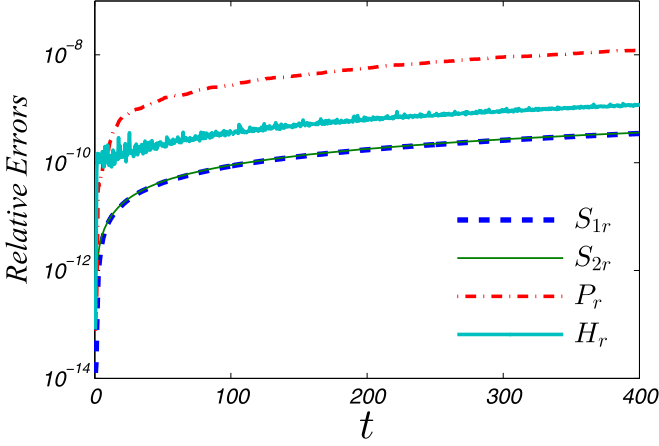
FIG. 8. Evolution of the relative errors of the mass S_r, momentum P_r, and Hamiltonian H_r for a specific realization of randomness.

APPENDIX A: NUMERICAL ERRORS

In this Appendix, we briefly discuss the numerical errors for our simulation results. The coupled system (1) has infinite numbers of conserved integrals over the evolution coordinate, with the first three being the mass, momentum, and Hamiltonian:

$$S_1 = \frac{1}{L} \int |\psi_1|^2 dx, \quad S_2 = \frac{1}{L} \int |\psi_2|^2 dx, \tag{A1a}$$

$$P = \frac{i}{L} \int \left(\psi_1 \frac{\partial \psi_1^*}{\partial x} - \psi_1^* \frac{\partial \psi_1}{\partial x} + \psi_2 \frac{\partial \psi_2^*}{\partial x} - \psi_2^* \frac{\partial \psi_2}{\partial x} \right) dx, \tag{A1b}$$

$$H = \frac{1}{L} \int \left[\left| \frac{\partial \psi_1}{\partial x} \right|^2 + \left| \frac{\partial \psi_2}{\partial x} \right|^2 - (|\psi_1|^2 + |\psi_2|^2)^2 \right] dx. \tag{A1c}$$

The preservation of these integrals can be checked by tracking their relative errors as $S_r(t) = |S(t) - S(0)|/|S(0)|$, $P_r(t) = |P(t) - P(0)|/|P(0)|$, and $H_r(t) = |H(t) - H(0)|/|H(0)|$. We present a typical result in Fig. 8, where we see that all the relative errors are considerably small. For our simulations, the errors are generally bounded at the level of less than 10^{-7}. Thus, the mass, momentum, and Hamiltonian are well conserved.

In addition, we have checked the time-invariance of the main spectra for specific realizations. The relative errors of all the IST eigenvalues at $t = 0$ and $t_f = 400$ are kept below the level of 10^{-4}, in which more than 90% of the eigenvalues have the relative errors less than 10^{-8}, and the errors for those with $|\eta| > 0.05$ are smaller than 10^{-6}. Thus, we can conclude that in our simulations the nonlinear spectra are well preserved with time increasing, as required by the integrability of the system.
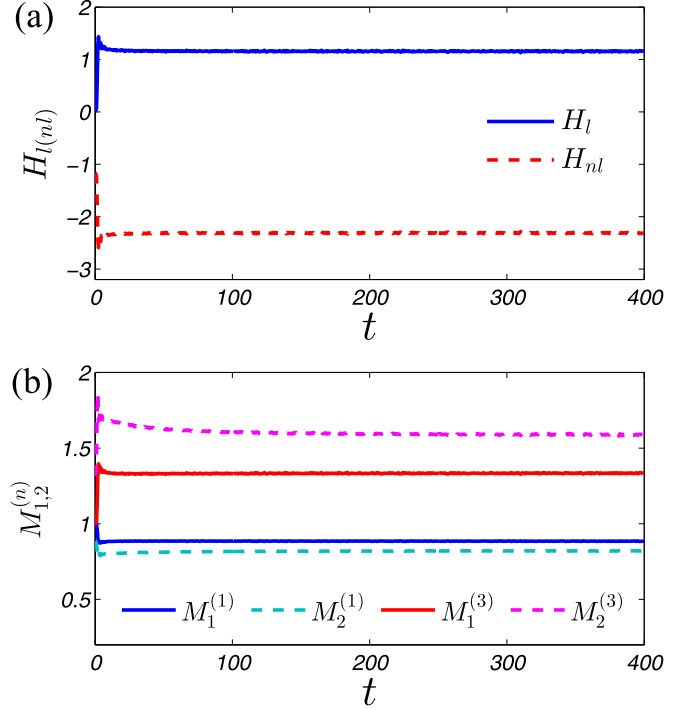

FIG. 9. (a) Time evolution of the ensemble-averaged kinetic (blue solid line) and potential energies (red dashed line). (b) The normalized moments averaged over different ensembles as functions of time. The blue solid line and light-blue dashed line correspond to the 1st moments for ψ_1 and ψ_2, while the red solid line and pink dashed line correspond to the 3rd moments. The parameters are the same as those in Fig. 2.

APPENDIX B: THE STATIONARY REGIME

We provide more numerical evidences to support the existence of the stationary regime for relatively long times. First, we check the ensemble-averaged kinetic energy $H_l = \langle \frac{1}{L} \int (|\partial \psi_1/\partial x|^2 + |\partial \psi_2/\partial x|^2) dx \rangle$ and potential energy $H_{nl} = \langle -\frac{1}{L} \int (|\psi_1|^2 + |\psi_2|^2)^2 dx \rangle$, with the results shown in Fig. 9(a). Second, we consider the ensemble-averaged 1st and 3rd normalized moments of the wave fields $M_j^{(1)} = \langle |\psi_j| \rangle / \langle |\psi_j|^2 \rangle^{\frac{1}{2}}$ and $M_j^{(3)} = \langle |\psi_j|^3 \rangle / \langle |\psi_j|^2 \rangle^{\frac{3}{2}}$, where $j = 1, 2$ is for different wave components. The time evolution of these moments are plotted in Fig. 9(b). All the statistical quantities indicate the same trend as in Fig. 2 that the IT may approach its stationary state after a short-time transient regime starting from the initial conditions.

We also present here the ensemble-averaged scintillation indices $\kappa(t)$ for several σ with different orders of magnitudes ($l_c = 2$), as seen in Fig. 10. This figure shows that the use of $t_0 = 200$ is appropriate in Eq. (4) since the wave fields in both components tend to their stationary states after this time.

APPENDIX C: AN EXAMPLE ON THE NONLINEAR SPECTRA

Through an example we show that the nonlinear spectra can be effectively obtained by either the DK scheme or FC method with a periodization of the wave field. Figure 11(a)
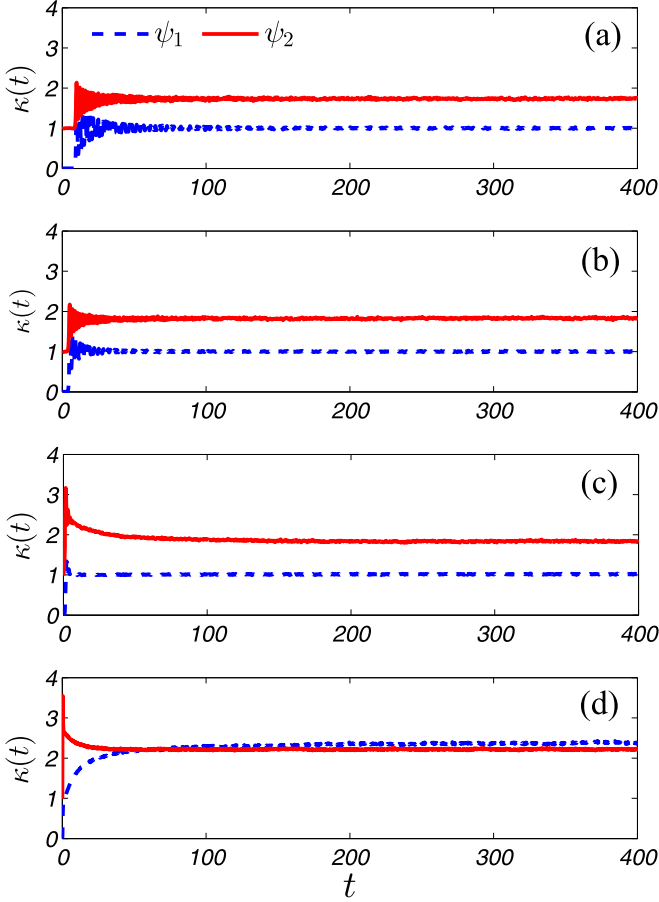
FIG. 10. Ensemble-averaged scintillation indices κ as functions of t for $l_c = 2$. (a) $\sigma = 0.0001$; (b) $\sigma = 0.01$; (c) $\sigma = 0.2$; (d) $\sigma = 0.84$. The blue dashed line is for the mode ψ_1 and the red solid line is for the mode ψ_2.

presents the wave profiles in a periodic box of size $L = 2\pi$, where we use a plane wave in one component and partially coherent humps in another component. Their nonlinear spectra by different schemes are given in Fig. 11(b), revealing the same global distribution of the eigenvalues composed of three main complex conjugate loops and a small-amplitude loop across the real axis. The distinction is that we have denser points of eigenvalues for the DK scheme since it is more computationally efficient than the FC method when the periodization is large.

APPENDIX D: FOURIER COLLOCATION METHOD ON SOME KNOWN SOLUTIONS

Hereby we demonstrate that the FC method (including the related DK scheme) works correctly on some known solutions of the Manakov model with vanishing or periodic boundary conditions.

The N-soliton solutions of Eq. (1) can be written explicitly as (the notations are the same as in Ref. [3])

$$\begin{pmatrix} \psi_1 \\ \psi_2 \end{pmatrix} = 2i \sum_{j,k=1}^{N} \begin{pmatrix} \alpha_j \\ \beta_j \end{pmatrix} e^{\theta_j - \theta_k^*} (M^{-1})_{jk}, \quad \text{(D1)}$$

where

$$\theta_k = -i\lambda_k x - 2i\lambda_k^2 t, \quad \text{(D2)}$$

and M is an $N \times N$ matrix with its elements given by

$$M_{jk} = \frac{1}{\lambda_j^* - \lambda_k} [e^{-(\theta_j^* + \theta_k)} + (\alpha_j^* \alpha_k + \beta_j^* \beta_k) e^{\theta_j^* + \theta_k}]. \quad \text{(D3)}$$

We first check the single-soliton solutions, where we set $N = 1$ in Eq. (D1). Letting $\lambda = \xi + i\eta$ and introducing the polarization vector $\mathbf{c} = (\alpha_1, \beta_1)^T / \sqrt{|\alpha_1|^2 + |\beta_1|^2}$, the solutions can be written as

$$(\psi_1, \psi_2)^T = \mathbf{c} \cdot 2\eta \operatorname{sech}[2\eta(x + 4\xi t + x_0)]e^{-2i\xi x - 4i(\xi^2 - \eta^2)t}. \quad \text{(D4)}$$

The polarization vector can control the relative power distribution between the two components of this solutions. We present two cases in Figs. 12(a)–12(f): One is for $\mathbf{c} = (1, 0)^T$ where the Manakov soliton is just the scalar NLS soliton and another one is for $\mathbf{c} = (0.6, 0.8)^T$, with the same spectral eigenvalue $\lambda = 0.25 + i$. For different power distribution, we see in Figs. 12(c) and 12(f) that this eigenvalue can be accurately calculated by using the FC method.

Second, we see the two-soliton solutions ($N = 2$) which describe the collision of two Manakov solitons. A redistribution of the power among the two components is a distinctive feature that does not occur for the scalar NLS solitons. We take $\lambda_1 = 0.1 + 0.7i$, $\lambda_2 = -0.1 + 0.7i$, $(\alpha_1, \alpha_2) = (1, 1)$, and $(\beta_1, \beta_2) = (0.25, 0)$, as plotted in Figs. 12(g) and 12(h). In Fig. 12(i), we present the eigenvalues computed by using the FC method, and find that the results fully agree.

Finally, we consider the Type I solitons with the same parameters as in Fig. 2 of Ref. [36]. This is the trivial vectorization of the breather solutions of the scalar NLS equation with finite background. Its spectrum consists of a segment $[-i, i]$ and discrete eigenvalues $\lambda = \pm 1.25i$. For the used parameters, we can employ the DK scheme with periodic boundary conditions. The spectrum was numerically solved, as provided in Fig. 12(l), where it completely accords with our expectation.

APPENDIX E: A COMPARABLE VIEW ON THE NONLINEAR SPECTRA

In this Appendix, we compare the nonlinear spectra between the Manakov model (see Figs. 5 and 6) and the scalar NLS equation with $\psi(x, 0) = f(x)$ [equivalent to the case of $\psi_1(x, 0) = 0$ and $\psi_2(x, 0) = f(x)$]. In Figs. 13(a) and 13(b), the global spectra for typical wave fields with $\sigma = 0.2$ and distinctive l_c ($l_c = 1$ and $l_c = 5$) are demonstrated. The zoomed pictures of the spectra near the origin are respectively shown in Figs. 13(c) and 13(d). For the scalar NLS equation, the small-amplitude bands across and near the real axis represent small linear waves and breather type structures. We see that most of the larger-amplitude nonlinear excitations correspond to the pointlike eigenvalue bands, which stand for the soliton-like objets. The distribution of these eigenvalues depends on the correlation length l_c when σ is fixed.

The main difference between the Manakov and scalar NLS spectra includes two aspects: (i) The vector case contains a
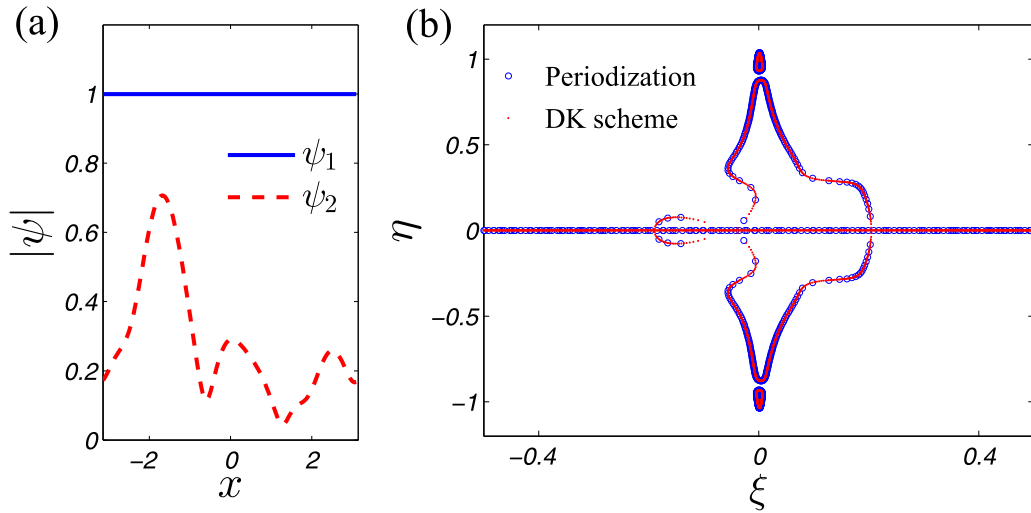
FIG. 11. (a) The profiles of a vector wave field $|\psi_1(x)|$ and $|\psi_2(x)|$ at $t = 0$ within a periodic box $[-\pi, \pi]$. (b) Comparison of the spectra computed respectively by the DK scheme (red dots, $\Delta\gamma = 1/500$) and FC method with a spatial periodization (blue circles, including 128 periods).
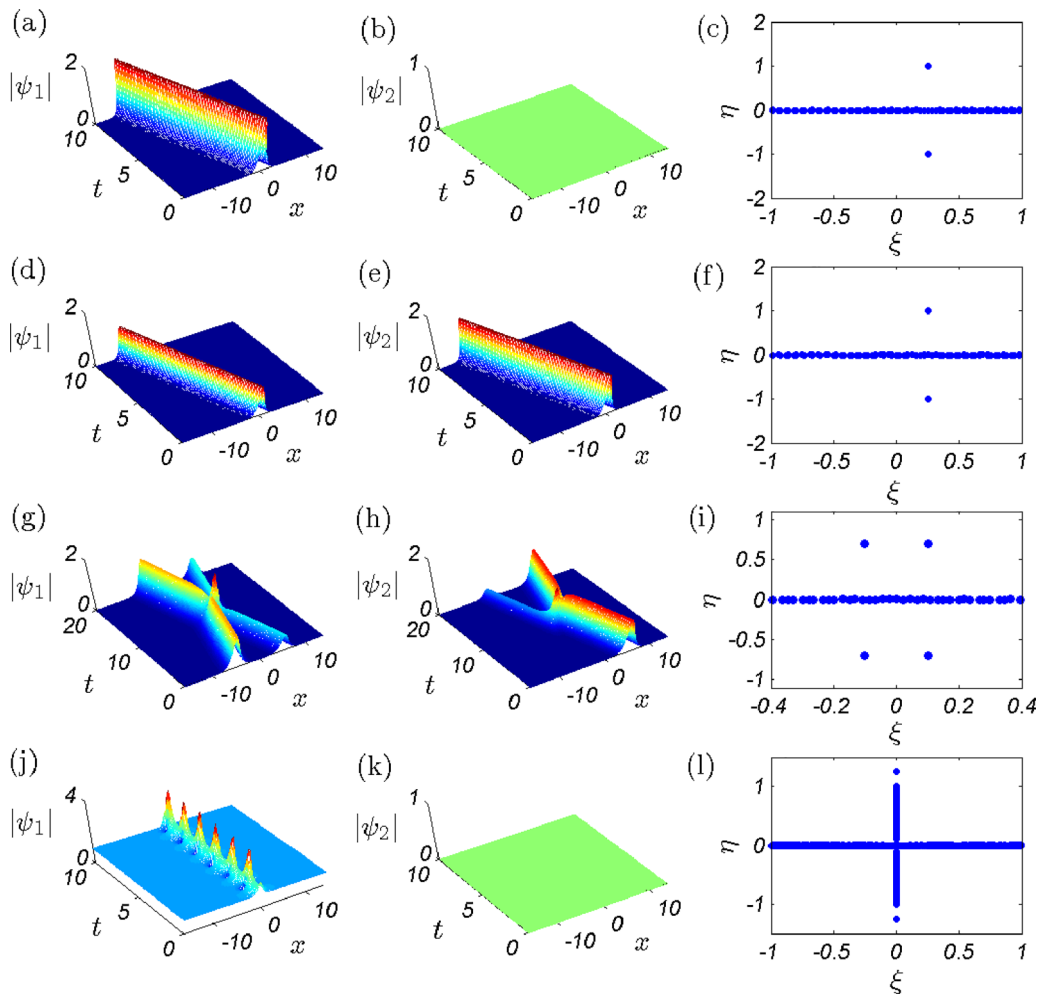

FIG. 12. Typical solitonic solutions of Manakov model (the left two columns) and their IST spectra computed by using the FC method (the right column). (a)–(c) The single-soliton solutions with $\lambda = 0.25 + i$ and $\mathbf{c} = (1, 0)^T$; (d)–(f) the single-soliton solutions with $\lambda = 0.25 + i$ and $\mathbf{c} = (0.6, 0.8)^T$; (g)–(i) the two-soliton solutions with $\lambda_1 = 0.1 + 0.7i$, $\lambda_2 = -0.1 + 0.7i$, $(\alpha_1, \alpha_2) = (1, 1)$, and $(\beta_1, \beta_2) = (0.25, 0)$; (j)–(l) the Type I soliton solutions with the same parameters as in Fig. 2 of Ref. [36].
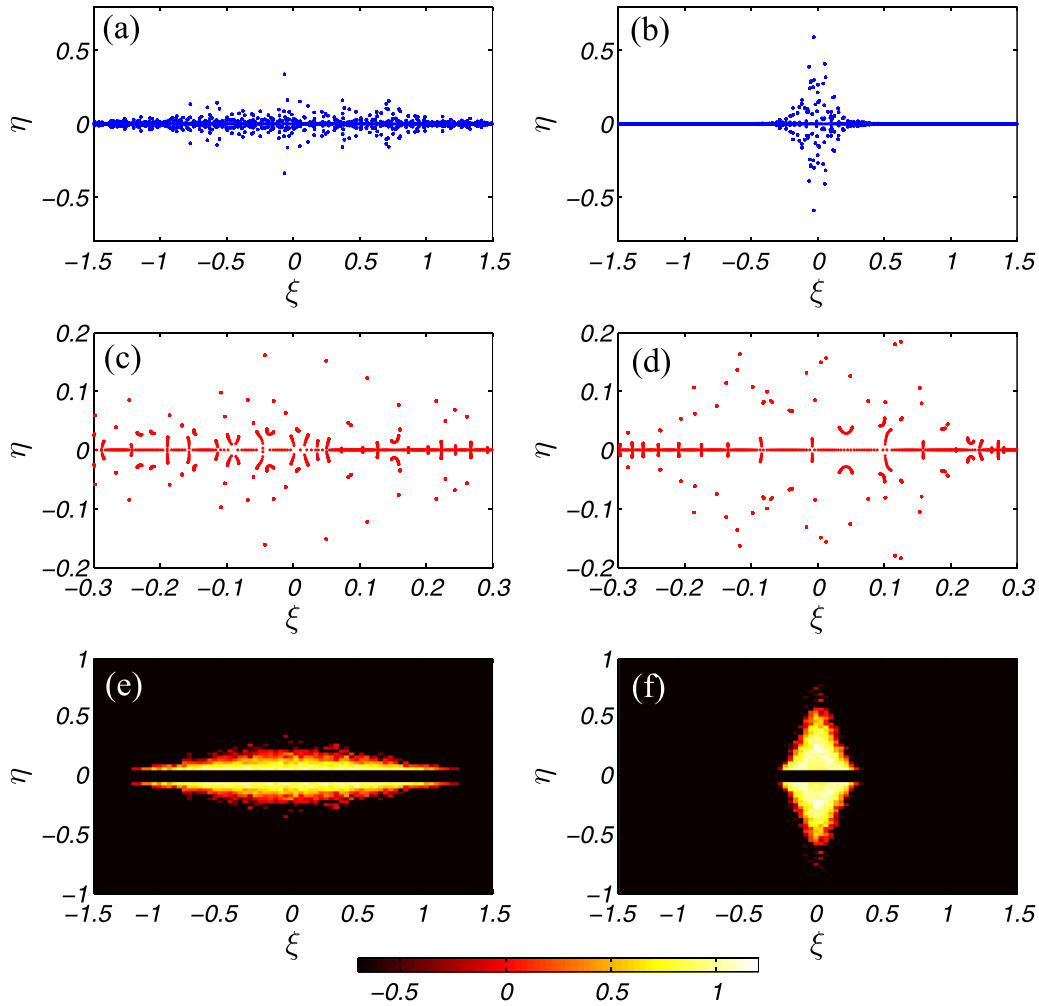
FIG. 13. The global spectra for typical scalar NLS wave fields with $\sigma = 0.2$ and (a) $l_c = 1$; (b) $l_c = 5$. The spectral distribution near the real axis is zoomed in panels (c) and (d), respectively. Logarithm plots of the probability density functions $\log_{10}[p(\xi, \eta)]$ for the main spectral eigenvalues of the scalar NLS equation with initial parameters $\sigma = 0.2$ and (e) $l_c = 1$; (f) $l_c = 5$. The statistics was taken from 100 realizations of the initial conditions.

large eigenvalue loop dominating the spectrum shape which is attributed to the addition of $\psi_1(x, 0) = 1$, while the scalar case does not have such a structure; (ii) the eigenvalues representing solitons locate near the point $\lambda = \pm i$ for the vector case, while the scalar case has a distinctive distribution.

In Figs. 13(e) and 13(f) we plot statistical distribution of the main spectral eigenvalues for the scalar NLS. As compared with those in Fig. 6, a remarkable difference on the global distribution can be seen due to the vectorization of the system.

[1] M. J. Ablowitz and H. Segur, *Solitons and the Inverse Scattering Transform* (SIAM, Philadelphia, PA, 1981).

[2] Y. S. Kivshar and B. A. Malomed, Dynamics of solitons in nearly integrable systems, Rev. Mod. Phys. **61**, 763 (1989).

[3] J. Yang, *Nonlinear Waves in Integrable and Nonintegrable Systems* (SIAM, Philadelphia, PA, 2010).

[4] A. R. Osborne, *Nonlinear Ocean Waves and the Inverse Scattering Transform* (Academic Press, San Diego, CA, 2010).

[5] V. E. Zakharov, Kinetic equation for solitons, Sov. Phys. JETP **33**, 538 (1971).

[6] G. A. El and A. M. Kamchatnov, Kinetic equation for a dense soliton gas, Phys. Rev. Lett. **95**, 204101 (2005).

[7] A. I. D'yachenko, V. E. Zakharov, A. N. Pushkarev, V. F. Shvets, and V. V. Yan'kov, Soliton turbulence in nonintegrable wave systems, Sov. Phys. JETP **69**, 1144 (1989).

[8] A. Picozzi and J. Garnier, Incoherent soliton turbulence in nonlocal nonlinear media, Phys. Rev. Lett. **107**, 233901 (2011).

[9] V. E. Zakharov, Turbulence in integrable systems, Stud. Appl. Math. **122**, 219 (2009).

[10] E. Pelinovsky and A. Sergeeva, Numerical modeling of the KdV random wave field, Eur. J. Mech. B Fluids **25**, 425 (2006).

[11] D. S. Agafontsev and V. E. Zakharov, Integrable turbulence and formation of rogue waves, Nonlinearity **28**, 2791 (2015).

[12] J. M. Soto-Crespo, N. Devine, and N. Akhmediev, Integrable turbulence and rogue waves: Breathers or solitons? Phys. Rev. Lett. **116**, 103901 (2016).

[13] N. Akhmediev, J. M. Soto-Crespo, and N. Devine, Breather turbulence versus soliton turbulence: Rogue waves, probability density functions, and spectral features, Phys. Rev. E **94**, 022212 (2016).

[14] P. Walczak, S. Randoux, and P. Suret, Optical rogue waves in integrable turbulence, Phys. Rev. Lett. **114**, 143903 (2015).

[15] P. Suret, R. E. Koussaifi, A. Tikan, C. Evain, S. Randoux, C. Szwaj, and S. Bielawski, Single-shot observation of optical rogue waves in integrable turbulence using time microscopy, Nat. Commun. **7**, 13136 (2016).

[16] S. Nazarenko, *Wave Turbulence* (Springer, Heidelberg, 2011).

[17] F. Copie, S. Randoux, and P. Suret, The Physics of the one-dimensional nonlinear Schrödinger equation in fiber optics: Rogue waves, modulation instability and self-focusing phenomena, Rev. Phys. **5**, 100037 (2020).

[18] A. Gelash, D. Agafontsev, V. Zakharov, G. El, S. Randoux, and P. Suret, Bound state soliton gas dynamics underlying the spontaneous modulational instability, Phys. Rev. Lett. **123**, 234102 (2019).

[19] A. Tikan, S. Bielawski, C. Szwaj, S. Randoux, and P. Suret, Single-shot measurement of phase and amplitude by using a heterodyne time-lens system and ultrafast digital time-holography, Nat. Photon. **12**, 228 (2018).

[20] A. E. Kraych, D. Agafontsev, S. Randoux, and P. Suret, Statistical properties of the nonlinear stage of modulation instability in fiber optics, Phys. Rev. Lett. **123**, 093902 (2019).

[21] S. Randoux, P. Walczak, M. Onorato, and P. Suret, Nonlinear random optical waves: Integrable turbulence, rogue waves and intermittency, Phys. D **333**, 323 (2016).

[22] D. S. Agafontsev, S. Randoux, and P. Suret, Extreme rogue wave generation from narrowband partially coherent waves, Phys. Rev. E **103**, 032209 (2021).

[23] C. Kharif and E. Pelinovsky, Physical mechanisms of the rogue wave phenomenon, Eur. J. Mech. B Fluids **22**, 603 (2003).

[24] K. Dysthe, H. E. Krogstad, and P. Müller, Oceanic rogue waves, Annu. Rev. Fluid Mech. **40**, 287 (2008).

[25] N. Akhmediev, J. M. Soto-Crespo, and A. Ankiewicz, Extreme waves that appear from nowhere: On the nature of rogue waves, Phys. Lett. A **373**, 2137 (2009).

[26] M. Onorato, S. Residori, U. Bortolozzo, A. Montinad, and F. T. Arecchi, Rogue waves and their generating mechanisms in different physical contexts, Phys. Rep. **528**, 47 (2013).

[27] J. M. Dudley, F. Dias, M. Erkintalo, and G. Genty, Instabilities, breathers, and rogue waves in optics, Nat. Photonics **8**, 755 (2014).

[28] A. Degasperis and S. Lombardo, Integrability in action: Solitons, instability, and rogue waves, in *Rogue and Shock Waves in Nonlinear Dispersive Media*, Lecture Notes in Physics, Vol. 926, edited by M. Onorato, S. Resitori, and F. Baronio (Springer, Cham, 2016).

[29] P. G. Kevrekidis, D. J. Frantzeskakis, and R. Carretero-González, *Emergent Nonlinear Phenomena in Bose-Einstein Condensates: Theory and Experiment*, Springer Series on Atomic, Optical, and Plasma Physics, Vol. 45 (Springer, Berlin, 2008).

[30] P. G. Kevrekidis and D. J. Frantzeskakis, Solitons in coupled nonlinear Schrödinger models: A survey of recent developments, Rev. Phys. **1**, 140 (2016).

[31] S. Chen, F. Baronio, J. M. Soto-Crespo, P. Grelu, and D. Mihalache, Versatile rogue waves in scalar, vector, and multi-dimensional nonlinear systems, J. Phys. A **50**, 463001 (2017).

[32] Z.-Y. Sun, Y.-T. Gao, X. Yu, W.-J. Liu, and Y. Liu, Bound vector solitons and soliton complexes for the coupled nonlinear Schrödinger equations, Phys. Rev. E **80**, 066608 (2009).

[33] Z.-Y. Sun, Y.-T. Gao, X. Yu, and Y. Liu, Dynamics of the Manakov-typed bound vector solitons with random initial perturbations, Ann. Phys. **327**, 1744 (2012).

[34] R. Ramakrishnan, S. Stalin, and M. Lakshmanan, Nondegenerate solitons and their collisions in Manakov systems, Phys. Rev. E **102**, 042212 (2020).

[35] S. Stalin, R. Ramakrishnan, and M. Lakshmanan, Nondegenerate bright solitons in coupled nonlinear Schrödinger systems: Recent developments on optical vector solitons, Photonics **8**, 258 (2021).

[36] D. Kraus, G. Biondini, and G. Kovačič, The focusing Manakov system with nonzero boundary conditions, Nonlinearity **28**, 3101 (2015).

[37] A. A. Raskovalov and A. A. Gelash, Resonant interactions of vector breathers, JETP Lett. **115**, 45 (2022).

[38] F. Baronio, A. Degasperis, M. Conforti, and S. Wabnitz, Solutions of the vector nonlinear Schrödinger equations: Evidence for deterministic rogue waves, Phys. Rev. Lett. **109**, 044102 (2012).

[39] F. Baronio, M. Conforti, A. Degasperis, and S. Lombardo, Rogue waves emerging from the resonant interaction of three waves, Phys. Rev. Lett. **111**, 114101 (2013).

[40] S. Chen, P. Grelu, and J. M. Soto-Crespo, Dark- and bright-rogue-wave solutions for media with long-wave-short-wave resonance, Phys. Rev. E **89**, 011201(R) (2014).

[41] S. V. Manakov, On the theory of two-dimensional stationary self-focusing of electromagnetic waves, Sov. J. Exp. Theor. Phys. **38**, 248 (1974).

[42] A. Mančić, F. Baronio, L. Hadžievski, S. Wabnitz, and A. Maluckov, Statistics of vector Manakov rogue waves, Phys. Rev. E **98**, 012209 (2018).

[43] X.-Y. Xie, S.-K. Yang, C.-H. Ai, and L.-C. Kong, Integrable turbulence for a coupled nonlinear Schrödinger system, Phys. Lett. A **384**, 126119 (2020).

[44] D. Pierangeli, M. Flammini, L. Zhang, G. Marcucci, A. J. Agranat, P. G. Grinevich, P. M. Santini, C. Conti, and E. DelRe, Observation of Fermi-Pasta-Ulam-Tsingou recurrence and its exact dynamics, Phys. Rev. X **8**, 041017 (2018).

[45] A. Safari, R. Fickler, M. J. Padgett, and R. W. Boyd, Generation of caustics and rogue waves from nonlinear instability, Phys. Rev. Lett. **119**, 203901 (2017).

[46] Z.-Y. Sun and X. Yu, Nearly integrable turbulence and rogue waves in disordered nonlinear Schrödinger systems, Phys. Rev. E **103**, 062203 (2021).

[47] Z.-Y. Sun and X. Yu, Nonlinear Schrödinger waves in a disordered potential: Branched flow, spectrum diffusion, and rogue waves, Chaos **32**, 023108 (2022).

[48] G. Roberti, G. El, S. Randoux, and P. Suret, Early stage of integrable turbulence in the one-dimensional nonlinear Schrödinger equation: A semiclassical approach to statistics, Phys. Rev. E **100**, 032212 (2019).

[49] S. K. Turitsyn, J. E. Prilepsky, S. T. Le, S. Wahls, L. L. Frumin, M. Kamalian, and S. A. Derevyanko, Nonlinear Fourier transform for optical data processing and transmission: Advances and perspectives, Optica **4**, 307 (2017).

[50] I. S. Chekhovskoy, O. V. Shtyrina, M. P. Fedoruk, S. B. Medvedev, and S. K. Turitsyn, Nonlinear Fourier transform for analysis of coherent structures in dissipative systems, Phys. Rev. Lett. **122**, 153901 (2019).

[51] F. Bonnefoy, A. Tikan, F. Copie, P. Suret, G. Ducrozet, G. Prabhudesai, G. Michel, A. Cazaubiel, E. Falcon, G. El, and S. Randoux, From modulational instability to focusing dam breaks in water waves, Phys. Rev. Fluids **5**, 034802 (2020).

[52] P. Suret, A. Tikan, F. Bonnefoy, F. Copie, G. Ducrozet, A. Gelash, G. Prabhudesai, G. Michel, A. Cazaubiel, E. Falcon, G. El, and S. Randoux, Nonlinear spectral synthesis of soliton gas in deep-water surface gravity waves, Phys. Rev. Lett. **125**, 264101 (2020).

[53] M. J. Ablowitz, B. M. Herbst, and C. M. Schober, Computational chaos in the nonlinear Schrödinger equation without homoclinic crossings, Physica A **228**, 212 (1996).

[54] A. M. Calini and T. A. Ivey, Connecting geometry, topology and spectra for finite-gap NLS potentials, Physica D **152-153**, 9 (2001).

[55] P. G. Grinevich and P. M. Santini, The finite gap method and the analytic description of the exact rogue wave recurrence in the periodic NLS Cauchy problem, Nonlinearity **31**, 5258 (2018).

[56] M. G. Forest, D. W. McLaughlin, D. J. Muraki, and O. C. Wright, Nonfocusing instabilities in coupled, integrable nonlinear Schrödinger PDEs, J. Nonlinear Sci. **10**, 291 (2000).

[57] B. Deconinck and J. N. Kutz, Computing spectra of linear operators using the Floquet-Fourier-Hill method, J. Comput. Phys. **219**, 296 (2006).

[58] C. P. Olivier, B. M. Herbst, and M. A. Molchan, A numerical study of the large-period limit of a Zakharov-Shabat eigenvalue problem with periodic potentials, J. Phys. A **45**, 255205 (2012).

[59] M. Kamalian, J. E. Prilepsky, S. T. Le, and S. K. Turitsyn, Periodic nonlinear Fourier transform for fiber-optic communications, Part I: Theory and numerical methods, Opt. Express **24**, 18353 (2016).

[60] S. Randoux, P. Suret, and G. El, Inverse scattering transform analysis of rogue waves using local periodization procedure, Sci. Rep. **6**, 29238 (2016).

[61] M. J. Ablowitz, B. Prinari, and A. D. Trubatch, *Discrete and Continuous Nonlinear Schrödinger Systems* (Cambridge University Press, Cambridge, UK, 2004).

[62] S. Lannig, C.-M. Schmied, M. Prüfer, P. Kunkel, R. Strohmaier, H. Strobel, T. Gasenzer, P. G. Kevrekidis, and M. K. Oberthaler, Collisions of three-component vector solitons in Bose-Einstein condensates, Phys. Rev. Lett. **125**, 170401 (2020).